Publication Year	2023
Acceptance in OA	2025-03-07T13:58:27Z
Title	Early Results from GLASS-JWST. XVII. Building the First Galaxies—Chapter 1. Star Formation Histories for 5 < z < 7 Galaxies
Authors	Dressler, Alan, VULCANI, Benedetta, Treu, Tommaso, Rieke, Marcia, Burns, Chris, CALABRO', Antonello, BONCHI, Andrea, CASTELLANO, Marco, FONTANA, Adriano, Leethochawalit, Nicha, Mason, Charlotte, MERLIN, Emiliano, Morishita, Takahiro, PARIS, Diego, Bradac, Marusa, MERCURIO, Amata, Nanayakkara, Themiya, POGGIANTI, Bianca Maria, SANTINI, Paola, Wang, Xin, Misselt, Karl, Stark, Daniel P., Willmer, Christopher
Publisher's version (DOI)	10.3847/2041-8213/ac9ebb
Handle	http://hdl.handle.net/20.500.12386/36517
Journal	THE ASTROPHYSICAL JOURNAL LETTERS
Volume	947

The Astrophysical Journal Letters, 947:L27 (15pp), 2023 April 20 https://doi.org/10.3847/2041-8213/ac9ebb

Early Results from GLASS-JWST. XVII. Building the First Galaxies—Chapter 1. Star Formation Histories for $5 < z < 7$ Galaxies

Alan Dressler[1], Benedetta Vulcani[2], Tommaso Treu[3], Marcia Rieke[4], Chris Burns[1], Antonello Calabrò[5], Andrea Bonchi[5,6], Marco Castellano[5], Adriano Fontana[5], Nicha Leethochawalit[7,8], Charlotte Mason[9,10], Emiliano Merlin[5], Takahiro Morishita[11], Diego Paris[5], Marusa Bradac[12,13], Amata Mercurio[14], Themiya Nanayakkara[15], Bianca M. Poggianti[2], Paola Santini[5], Xin Wang[11], Karl Misselt[4], Daniel P. Stark[4], and Christopher Willmer[4]

[1] The Observatories, The Carnegie Institution for Science, 813 Santa Barbara St., Pasadena, CA 91101, USA; dressler@carnegiescience.edu
[2] INAF Osservatorio Astronomico di Padova, vicolo dell'Osservatorio 5, I-35122 Padova, Italy
[3] Department of Physics and Astronomy, University of California, Los Angeles, 430 Portola Plaza, Los Angeles, CA 90095, USA
[4] Steward Observatory, University of Arizona, 933 N. Cherry Ave., Tucson, AZ 85721, USA
[5] INAF Osservatorio Astronomico di Roma, Via Frascati 33, I-00078 Monteporzio Catone, Rome, Italy
[6] ASI-Space Science Data Center, Via del Politecnico, I-00133 Roma, Italy
[7] School of Physics, University of Melbourne, Parkville 3010, VIC, Australia
[8] ARC Centre of Excellence for All Sky Astrophysics in 3 Dimensions (ASTRO 3D), Australia
[9] Cosmic Dawn Center (DAWN), Denmark
[10] Niels Bohr Institute, University of Copenhagen, Jagtvej 128, DK-2200 Copenhagen N, Denmark
[11] Infrared Processing and Analysis Center, Caltech, 1200 E. California Blvd., Pasadena, CA 91125, USA
[12] University of Ljubljana, Department of Mathematics and Physics, Jadranska ulica 19, SI-1000 Ljubljana, Slovenia
[13] Department of Physics and Astronomy, University of California Davis, 1 Shields Ave., Davis, CA 95616, USA
[14] INAF–Osservatorio Astronomico di Capodimonte, Via Moiariello 16, I-80131 Napoli, Italy
[15] Centre for Astrophysics and Supercomputing, Swinburne University of Technology, PO Box 218, Hawthorn, VIC 3122, Australia
Received 2022 August 8; revised 2022 October 7; accepted 2022 October 30; published 2023 April 24

Abstract

The JWST observations of high-redshift galaxies are used to measure their star formation histories—the buildup of stellar mass in the earliest galaxies. Here we use a novel analysis program, SEDz*, to compare near-IR spectral energy distributions for galaxies with redshifts $5 < z < 7$ to combinations of stellar population templates evolved from $z = 12$. We exploit NIRCam imaging in seven wide bands covering 1–5 μm taken in the context of the GLASS-JWST-ERS program and use SEDz* to solve for well-constrained star formation histories for 24 exemplary galaxies. In this first look, we find a variety of histories, from long, continuous star formation over $5 < z < 12$ to short but intense starbursts, sometimes repeating, and, most commonly, contiguous mass buildup lasting ~0.5 Myr, possibly the seeds of today's typical M^* galaxies.

Unified Astronomy Thesaurus concepts: Galaxies (573); Galaxy evolution (594); High-redshift galaxies (734)

1. Introduction: Star Formation Histories: Building the First Galaxies

The buildup of stellar mass in a galaxy is expressed as its star formation history (SFH), that is, the rate of star formation over an epoch of cosmic time. Measuring the SFHs of galaxies over cosmic time has been a long-sought goal of extragalactic astronomy, extending back at least as far as the 1950s (Baade 1951). The best and most direct method, measuring the Hertzsprung–Russell diagrams of populations of stars for our own galaxy and its nearest neighbors—spectacularly advanced by the Hubble Space Telescope (HST; e.g., Tosi et al. 1989; Gallart et al. 1996; Tolstoy & Saha 1996; Aparicio & Hidalgo 2009; Cignoni & Tosi 2010)—is unfortunately limited to a number of present-day galaxies (e.g., Dalcanton et al. 2009, 2012) in the local universe.

To look back in time to galaxies at cosmic distances has been critically challenging because unresolved stellar populations cannot constrain SFHs for ages older than 2 Gyr, beyond which the dependence of an integrated spectrum on age and metallicity thwarts any comprehensive analysis (e.g., Worthey 1994). The ability to resolve SFHs over <2 Gyr of "lookback" is due to the rapid evolution of light-dominating A stars over this time period (Dressler & Gunn 1983), resulting in a tight correlation of SFH and spectral energy distribution (SED) that quickly vanishes for ages $\tau > 2$ Gyr (see also Poggianti et al. 1999). The discovery of "late bloomer galaxies"—i.e., galaxies with rising SFRs (rather than falling as conventionally described; Dressler et al. 2018)—made use of this by observing the growth of galaxies from $z \sim 0.75$ to 0.45, a significant (2 Gyr) fraction of their lifetimes. The prevailing model for SFHs has been for homologous lognormal forms (Gladders et al. 2013; rapidly rising and slowly declining) over a Hubble time (Diemer et al. 2017), but Dressler et al. (2018) found that ~25% of Milky Way–mass galaxies more than doubled their mass during this relatively late period in cosmic history. This study made clear that the SFHs of the first billion years of star formation, $5 < z < 20$, would greatly benefit from the strong correlation of SED and SFH. Therefore, the potential of the James Webb Space Telescope (JWST) to produce such data has been eagerly awaited (see, e.g., Tacchella et al. 2022, for state-of-the-art HST-based work).

In this paper, we show very early results of this potential through the analysis of $5 < z < 7$ SEDs derived from seven-

band NIRCam images obtained as part of the GLASS-JWST Early Release Science program (Treu et al. 2022a). We start from the fluxes for ∼6600 galaxies extracted by Merlin et al. (2022, Paper II) in NIRCam parallel observations of NIRISS spectroscopy of the cluster A2744. We here exploit a program written expressly for the purpose of reconstructing the histories of galaxies at $5 < z < 7$ from the rich information encoded in their SEDs for the first time on real data. A recent paper by Whitler et al. (2023) applies similar techniques to JWST data of galaxies at $z > 8$, when the universe was less than 500 Myr old. By focusing on a sample at slightly lower redshift, we have access to redder rest-frame wavelengths and give sufficient time for older stellar populations to emerge.

These first results demonstrate that this technique will be a powerful tool in studying and understanding the buildup of stellar mass—the growth—of the first galaxies in our universe.

The paper is organized as follows. Section 2 and Appendix A explain and summarize the methodology in advance of a forthcoming paper that will provide more detail. Section 3 presents the observations and the selection of the sample. Section 4 shows 24 examples of the SEDs of $5 < z < 7$, with a focus on examples of various SFHs that we find—mainly long and short falling SFHs and prominent bursts. We describe the character of these SFHs and comment on the fidelity and robustness of the results, aided by Appendixes B and C, which also investigate the reliability of our identifications. Section 5 briefly contemplates the bounty expected from deeper, wider surveys already on the JWST observing schedule.

A standard cosmology with $\Omega_m = 0.3$, $\Omega_\Lambda = 0.7$, and $H_0 = 70$ km s^{-1} Mpc^{-1} is adopted.

2. Deriving the SFHs of the First Galaxies from NIRCam Photometry

The method we apply to derive SFHs follows the work of Kelson et al. (2016), who developed a maximum-likelihood Python code to deconstruct observed SEDs from the Carnegie-Spitzer-IMACS Survey (Kelson et al. 2014), in terms of best-fit stellar population templates. The program proved particularly effective in isolating the light from younger (<2 Gyr) populations of A stars, confirming an early photometric study (Oemler et al. 2013) that showed that 25% of Milky Way–mass galaxies at $z \sim 0.5$ had rising SFRs (rather than falling at $z < 1$, as conventionally described), producing at least 50% of their stellar mass in the previous 2 Gyr—so-called "late bloomers."

Dressler has followed this approach by writing SEDz*, a Fortran code for analyzing stellar populations for $z > 5$ galaxies, all of which have stellar ages of <1 Gyr. It was developed to answer a basic question: what do the SFHs of the earliest galaxies look like? That is, its purpose is to quantify SFHs—their forms—for a sample of very young galaxies. Other codes measure SFHs, of course, for example, PROSPECTOR (Johnson et al. 2021), EAZY (Brammer et al. 2008), and BEAGLE (Chevallard & Charlot 2016). They are essential tools in the study of galaxy evolution; they can provide information on many properties and behaviors for galaxies over a wide range of cosmic histories. The SEDz* program was developed to focus on SFHs over a special epoch. It takes advantage of a unique astrophysical opportunity: the light from galaxies in the first billion years is dominated by A stars, and A stars are the best clock for studying young stellar populations (Dressler & Gunn 1983; Couch & Sharples 1987). Because they evolve rapidly over a gigayear, the SFHs of A star–dominated populations can be derived (rather than inferred) from SEDs, and vice versa. There are no complexities; in addition to providing the proper clock, A stars are among the simplest stars (Morgan & Keenan 1973), main-sequence stars with relatively simple atmospheres. Hydrogen absorption dominates the opacity, not metal lines, thereby much reducing the influence of metal abundance and the environments of star formation. These are significant advantages for SEDz* in measuring SFHs during the first billion years of cosmic history.

Operationally, the data inputs to SEDz* are SEDs—flux measurements in NIRCam's wide bands.[16] The SEDz* program uses a nonnegative least-squares (NNLS) engine (Lawson & Hanson 1995), which combines custom star formation templates based on work by Robertson et al. (2010) and further developed by Stark et al. (2013[17]; see Section 3) and is used by the NIRCam team to simulate observations of galaxies in the GTO deep fields (Williams et al. 2018). The custom templates made for SEDz* cover the redshift range $3 < z < 12$.[18] For each template, there is a starting redshift with fluxes proportionate to stellar mass along with the evolution of this template, that is, the expected fluxes when observing that stellar population at subsequent epochs. The program divides the $3 < z < 12$ epoch into integer steps (i.e., 12, 11, 10, ..., 3) and operates with two sets of SED templates; one set is for 10 Myr bursts starting at epochs $5 < z < 12$, and the other is for continuous star formation (CSF) starting at redshifts as early as $z = 10$ but not after $z = 4$.

The process is to build up the stellar population by combining templates, epoch by epoch. For each step, NNLS works to improve the fit of combined fluxes to the observed SED, with each step evolving the preceding star formation forward and adding the fluxes of subsequent populations, like building a wave. For example, starting with a single 10 Myr burst at $z = 12$, SEDz* uses NNLS to find the mass that minimizes the χ^2 $\tilde{\chi}^2$ of the fit to the observed SED. Next, using the template of the $z = 12$ burst evolved to $z = 11$ and adding a population starting at $z = 11$, NNLS finds the stellar mass for each epoch (as small as zero) that further lowers the $\tilde{\chi}^2$. The process continues for bursts at 10, 9, ..., 5 and adds potential CSF populations (in units of 1.0 $M_\odot$ yr^{-1} over the z-integer-bound epoch) starting at $z = 10$ and as late as $z = 4$, again, as needed to improve the fit of the composite stellar populations to the observed SED. Detecting a CSF population defines the epoch of observation (OE) and ends the possibility of later bursts. To summarize, from $z = 12$ to 4, a sum of bursts and the possible onset of CSF improves the goodness of fit of the model-to-observed SED, measured as reduced $\tilde{\chi}^2$.

The SEDz* program does not prejudge the SFH. By using a combination of individual bursts and CSF templates, SEDz* has the flexibility to describe rising or declining, as well as bursty, SFHs. Whatever the elements contributing to the best fit to the observed SED, there is no preference or bias for any particular history. The SEDz* program provides error bars for

[16] F090W, F115W, F150W, F200W, F277W, F356W, and F444W. Fluxes were also calculated for F335M and F410M as part of the NIRCam GTO program, but these nonindependent bands were not used in the fitting here because they are not available in GLASS-JWST.

[17] The templates are based on Bruzual & Charlot (2003) models but include emission and nonstellar continuum from star-forming regions in calculating the fluxes.

[18] No reliable templates are available at higher redshift, and the resolution in redshift is likely too fine to use SEDz* for studying SFHs.

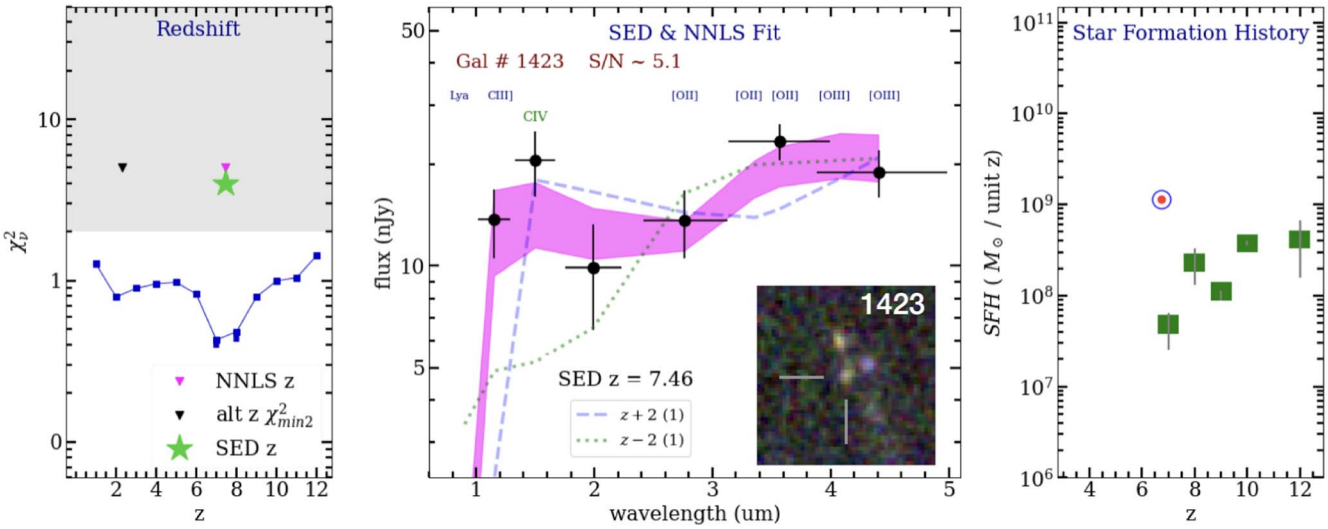

Figure 1. Example of the main output of the SEDz* code run on galaxy 1423, which has an S/N of 5.1. The three panels show the observed SED from the seven-band NIRCam imaging and NNLS fit (middle), the run of $\tilde{\chi}^2$ for the fit (left), and the SFH corresponding to the best fit (right). In the middle panel, the SEDz* fit is the magenta band, showing the "quartile range" of 21 trials, with observed fluxes perturbed by 1σ random errors. The positions of prominent emission lines are indicated in blue labels above the SED, with a larger green font marking a possible detection by excess compared to the best fit. (C IV is highlighted here, though its detection is marginal.) The dashed purple line and green dotted line show NNLS fits at $z+2$ and $z-2$, respectively, which are the values straddling the dip in $\tilde{\chi}^2$ seen in the left panel. In the inset, the color composite image of the galaxy, based on the long-wavelength camera (B = F277W, G = F356W, R = F444W), is shown. The RGB image is 3″ on a side. Left: run of $\tilde{\chi}^2$ for the SEDz* fit, with the primary minimum and a secondary minimum, if detected, marked by magenta and black triangles, respectively. The preferred redshift, marked with a green star, corresponds to the prominent drop in $\tilde{\chi}^2$ at $z \sim 7$. Right: SFH for this NNLS solution. Green boxes mark the mass contributed at each epoch. The bars are quartile errors in mass that arise from the random flux errors of the 21 models. Systematic errors in general should be comparable in magnitude to random errors and unlikely to significantly change the SED shape and, with it, the SFH (see text). The red dot in the blue circle marks the mass accumulated through the OE.

each mass point in the SFH. If they are large enough, multiple histories are possible, but this is not the case here. This means that, for a sample like this one, each SFH generated by SEDz* is unique; it is not meaningful to ask if another SFH would fit as well or better. With SEDz*, the minimum $\tilde{\chi}^2$ solution defines the SFH; there are no additional indicators or diagnostics of whether this is the "real" SFH or not.[19]

In this first exploration, we neglect the potential impact of dust. We will revisit the issue in future papers, when we will analyze larger samples in detail. However, we point out that most of the mass we find in running SEDz* on the present data is in comparatively old populations (hundreds of megayears), for which dust is not likely. In support of this, we notice that galaxies in our sample seem to be well described by SEDs with minimal dust, even for the youngest populations, and do not resemble the strong attenuation of ultraviolet light that is characteristic of populations with even moderate amounts of dust. Our choice is consistent with the results of several papers that show these initial JWST selected samples are uniformly blue (Nanayakkara et al. 2022, Paper XVI) and fairly dust-free (see Finlator et al. 2011; Jaacks et al. 2018; Mason et al. 2022, for a theoretical perspective), except for a few rare examples (Barrufet et al. 2022).

As discussed below, the main outputs of SEDz* are redshifts and SFHs.[20] To evaluate the performance in determining redshifts, a simulated catalog of galaxies following the distribution of Williams et al. (2018) was prepared in the context of the JWST Data Challenge 2 (DC2) to exercise the GTO pipeline. Simulated NIRCam images of many deep fields were created to test a wide range of analysis tools, with SEDz* among them. Although redshift recovery is not its purpose, SEDz* is competitive with the commonly used photo$z$ codes (based on DC2 results), even to the extent of identifying $z < 3$ galaxies, something SEDz* was not designed to do and is actually outside its native ability (because stellar populations exceed an age of 1 Gyr).

To test the performance of SEDz* on SFHs, a code that accepts parametric SFHs or generates stochastic SFHs was written and applied to the DC2 sample; SEDz* was found to recover declining SFHs, as well as single and multiple bursts of star formation, with good fidelity but exhibiting a limited dynamic range for SFHs rising from higher redshift, as would be expected (older populations are fading while younger populations ascend). Examples of these simulations are given in Appendix A, along with a description of how SEDz* is used to make these tests that provides further insight into how the program works.

A more detailed description of the features of the code and experience in its development, along with the results of DC2 and further SFH tests, is planned for a forthcoming paper (A. Dressler et al. 2022, in preparation). The SEDz* program has passed its early tests of measuring redshifts and SFHs; the purpose of this paper is to demonstrate its potential by applying it to some of the first real data from GLASS-JWST.

3. Observations and Data Sample

We use the NIRCam data obtained on 2022 June 28–29 in the context of the GLASS-JWST-ERS survey (Treu et al. 2022a). They consist of images centered at R.A. = 3°.5017025 and decl. = −30°.3375436 and taken in seven wide filters: F090W, F115W, F150W, F200W, F277W, F356W, and F444W. The 5σ depths in a 0″.30 diameter aperture are in

[19] The SEDz* program is similar to the "nonparametric" mode of PROSPECTOR (Johnson et al. 2021), in that it does not require simplified assumptions about the functional form of the SFH that are common in other methods (Chevallard & Charlot 2016).

[20] The SFHs derived from broadband photometry have resolutions of tens of megayears, compared to the 10 Myr or better resolution using spectroscopic data.

Table 1
Summary of the Main Galaxy Properties of the Sample Discussed in the Paper

ID	R.A. (J2000)	Decl. (J2000)	z	F444w (μJy)	$\log(M_*)$ ($M_\odot$)	Notes
1423	00:14:03.29	−30:21:46.7	7.5	0.019 ± 0.003	9.1	
733	00:14:01.51	−30:22:12.6	6.5	0.031 ± 0.004	9.5	L
2199	00:14:04.77	−30:21:14.8	6.9	0.046 ± 0.003	9.5	L
3459	00:14:01.05	−30:17:41.7	5.7	0.032 ± 0.004	9.4	L
3665	00:14:00.96	−30:18:00.8	5.2	0.019 ± 0.003	9.0	L
4761	00:13:58.16	−30:19:23.5	6.4	0.094 ± 0.005	9.7	L, (2)
5429	00:13:58.11	−30:19:03.9	7.0	0.023 ± 0.004	9.2	L
5879	00:13:54.26	−30:18:51.8	5.1	0.018 ± 0.003	8.9	L
6155	00:14:02.99	−30:18:47.8	6.8	0.012 ± 0.003	9.2	L
4144	00:14:02.29	−30:18:31.9	5.9	0.024 ± 0.004	9.2	L, *
483	00:14:05.72	−30:22:22.5	6.5	0.036 ± 0.004	9.2	B, *
1663	00:14:04.39	−30:21:38.5	5.6	0.007 ± 0.002	8.3	B, *
2104	00:14:02.85	−30:21:19.3	5.6	0.037 ± 0.003	9.1	B, *
2321	00:14:06.58	−30:21:18.2	5.8	0.014 ± 0.003	9.0	B, *
2626	00:14:04.50	−30:20:58.6	6.2	0.056 ± 0.004	9.1	B, *
2827	00:14:03.49	−30:20:51.0	5.6	0.013 ± 0.003	8.7	B, *
2850	00:14:03.02	−30:20:49.0	5.9	0.026 ± 0.004	9.3	B
2993	00:14:00.58	−30:20:40.8	6.7	0.021 ± 0.003	9.1	B
3824	00:13:53.63	−30:18:09.7	6.6	0.019 ± 0.003	9.0	B
3918	00:14:02.51	−30:18:15.2	5.5	0.016 ± 0.003	8.8	B
4026	00:13:52.80	−30:18:21.8	5.7	0.198 ± 0.008	9.8	B, (2)
4587	00:14:02.65	−30:19:16.2	5.7	0.028 ± 0.004	9.1	B
4736	00:14:02.01	−30:19:22.6	6.3	0.012 ± 0.002	8.6	B
5394	00:14:00.89	−30:19:04.7	6.3	0.076 ± 0.005	9.3	B, *
6324	00:14:01.78	−30:18:13.3	6.6	0.054 ± 0.004	9.4	B
680	00:14:05.63	−30:22:14.9	5.0	0.02 ± 0.003	8.9	S
1105	00:14:01.61	−30:21:58.6	5.4	0.077 ± 0.002	8.6	S
1127	00:14:02.43	−30:21:57.6	5.6	0.009 ± 0.002	8.8	S
1356	00:14:04.14	−30:21:48.7	5.0	0.017 ± 0.003	8.6	S
2006	00:13:59.17	−30:21:23.8	5.7	0.013 ± 0.003	8.8	S
2838	00:14:02.83	−30:20:48.6	6.7	0.13 ± 0.005	9.6	S, (1)
2864	00:14:05.89	−30:20:47.9	6.4	0.062 ± 0.005	9.4	S, (2)
2872	00:14:03.49	−30:20:51.0	5.6	0.013 ± 0.002	8.7	S
4455	00:14:00.00	−30:19:10.3	5.1	0.036 ± 0.006	9.2	S, *

Note. L: galaxies shown in Figure 3. B: galaxies shown in Figure 4. S: galaxies shown in Figure 5. (1) Galaxy also in the sample selected in Paper X; estimated redshifts are consistent within the uncertainties. (2) Galaxies also in the sample of Paper XVI; estimated redshifts are consistent within the uncertainties. Asterisk: galaxies not shown in the figures.

the range 29–29.5 AB mag. The final images are PSF-matched to the F444W band.

Details of the NIRCam data quality, reduction, and photometric catalog creation can be found in Paper II. As in other papers of this focus issue, we neglect the potential impact of lensing magnification, which is expected to be modest at the location of the NIRCam parallel field. We will revisit lensing magnification in future work. However, we note that the effect is small, and that lensing cannot affect SFH shapes, only their magnitude.

Out of the 6590 detections, we select sources with a signal-to-noise ratio (S/N) >5. This S/N is obtained by averaging the S/N of three bands: F200W, F277W, and F356W. We run SEDz* on this sample and obtain a redshift for all of the sources. From now on, we consider only galaxies with $5 < z < 7$, for a total of 123 objects.[21] We visually inspect the photometry of these galaxies, removing those with artifacts or chip boundaries affecting them in at least one band. We also select only galaxies with an SEDz* fit ($\tilde{\chi}^2 < 2$), for a total of 43 galaxies. We further reject 10 galaxies with clear (single-band) photometry errors, poor fits of the SED, or ambiguous $\tilde{\chi}^2$ (redshift) measurements. From the remaining 33, we select 24 that best illustrate the distribution and diversity of SFHs we find.[22]

4. First Results: Sample SFHs of the First Galaxies

In this section, we investigate a sample of SEDs from the JWST-GLASS NIRCam observations. By way of example, Figure 1 shows the SED of galaxy 1423 from the GLASS catalog of Paper II. This galaxy has a redshift of $z = 7.5$, so it does not enter the sample, but it is otherwise indistinguishable

[21] Galaxies at $z > 7$ are discussed in the companion papers by Castellano et al. (2022), Leethochawalit et al. (2022), Santini et al. (2022), Treu et al. (2022b), and Yang et al. (2022).

[22] Of the nine galaxies not shown, seven were equivalent to the burst examples of Figure 4, and one each resembled the samples of Figures 3 and 5. A statistical assessment of the frequency of each SFH shape requires a larger sample and is left for future work. Those galaxies are listed in Table 1. These are used in the following section to demonstrate the strength of the SFH reconstruction and the variety we find.

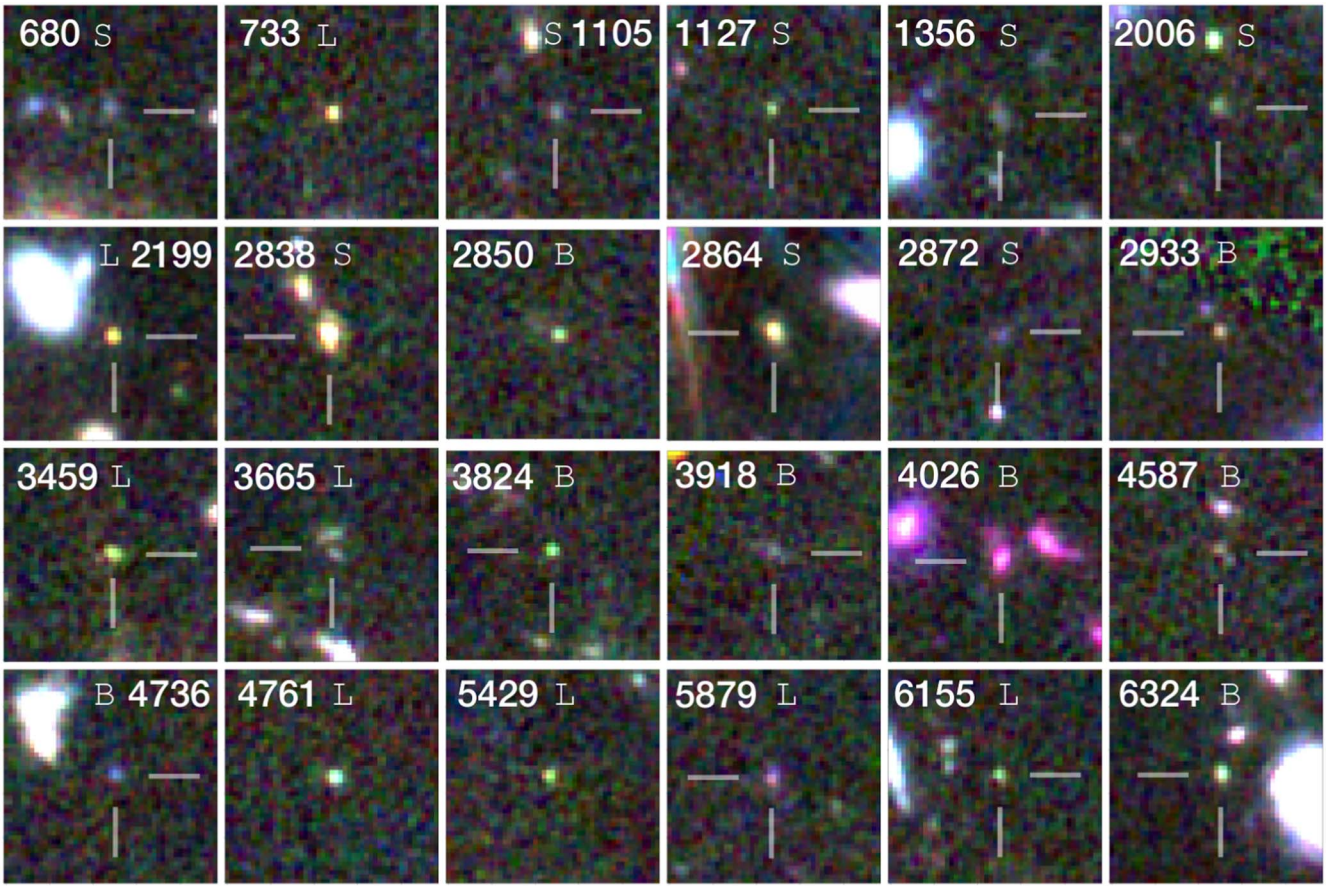

Figure 2. Color composite image based on the long-wavelength camera (B = F277W, G = F356W, R = F444W) for the 33 galaxies discussed in detail in this paper. Individual images are degraded to the lower resolution of F444W. Postage stamps are 3″ on a side. Pixels are 63 mas. The letter next to ID identifies the main characteristic of the SFH: S = short, L = long, and B = bursty.

from the 33 galaxies we have chosen and a good example to show the potential of SEDz* on a wide range of observations.

The data for galaxy 1423 are shown in three panels, the format for SEDz* results. The middle panel shows the SED, with crosses marking the fluxes with seven NIRCam "wide" filters in nJy, with errors. The SEDz* program has been run as described in the previous section on this SED, yielding the reduced $\tilde{\chi}^2$ distribution shown in the left panel, with a well-defined minimum at $z \approx 7.5$, between the two lowest points. Although SEDz* calculates the SED fit in integer redshifts, there is sufficient precision in the fits to interpolate between adjacent values; the first decimal in the redshifts is significant. Returning to the middle panel, the magenta band that "connects" the points is generated by randomly perturbing the input SED with 1σ flux errors (typically a few nJy) and repeating the NNLS fitting 21 times. The width of the band represents the quartile range of NNLS fits with this relatively low-S/N example. The run of $\tilde{\chi}^2$ presented in the left panel shows a significant drop between $z = 6$ and 7, interpolated by the program to derive the $z = 7.5$ value recorded in the central panel, in reasonable agreement with the estimate of the redshift as 6.9 obtained with the code EAzY (Brammer et al. 2008) with the default V1.3 spectral template and a flat prior in Paper X.

The real payoff for these data and our methodology is the SFH shown in the right panel; the green boxes record the stellar mass added to the galaxy at succeeding epochs. Error bars for these boxes do not include probable systematic errors (for example, the errors associated with photometry at these faint levels), but the relative uniformity of this clearly declining rate of star formation suggests that they are not severely underestimated. As we will see, this slowly falling SFH, starting at $z = 12$ (and likely earlier), shows a combination of features we find in this early study, both parametric and stochastic. The total mass of 10^9 $M_\odot$ is shown at $z = 7.5$, with the OE marked by the red dot/blue circle, while the squares showing the mass buildup are at their integer redshifts by necessity. The galaxy shows a factor of ∼3 buildup in stellar mass added after its formation at $z \sim 12$. This relatively low mass is consistent with the 10–20 nJy fluxes measured for standard mass-to-light ratios (Santini et al. 2022, Paper XI).

We continue by showing the SEDs of 24 galaxies chosen to illustrate the full sample. The details of such galaxies are given in Table 1, while color composite cutouts are presented in Figure 2.

Figure 3 shows a selection of eight galaxies at $5 < z < 7$ that display long, often continuous star formation back to $z \sim 11$–12 —early times in galaxy building. Unsurprisingly, then, these SFHs are either level or declining, remarkably steady for such an early birth and growth. Their total mass is typically a few billion $M_\odot$, with only one (4761) approaching 10^{10} $M_\odot$. Though they resemble the smooth, settled SFHs of much older galaxies, these SFHs are not the most common in our sample, accounting for only 27% of our sample.

These galaxies with extended SFHs straddle the end of reionization (Fan et al. 2006; Planck Collaboration et al. 2016), a full gigayear since the probable beginning of galaxy

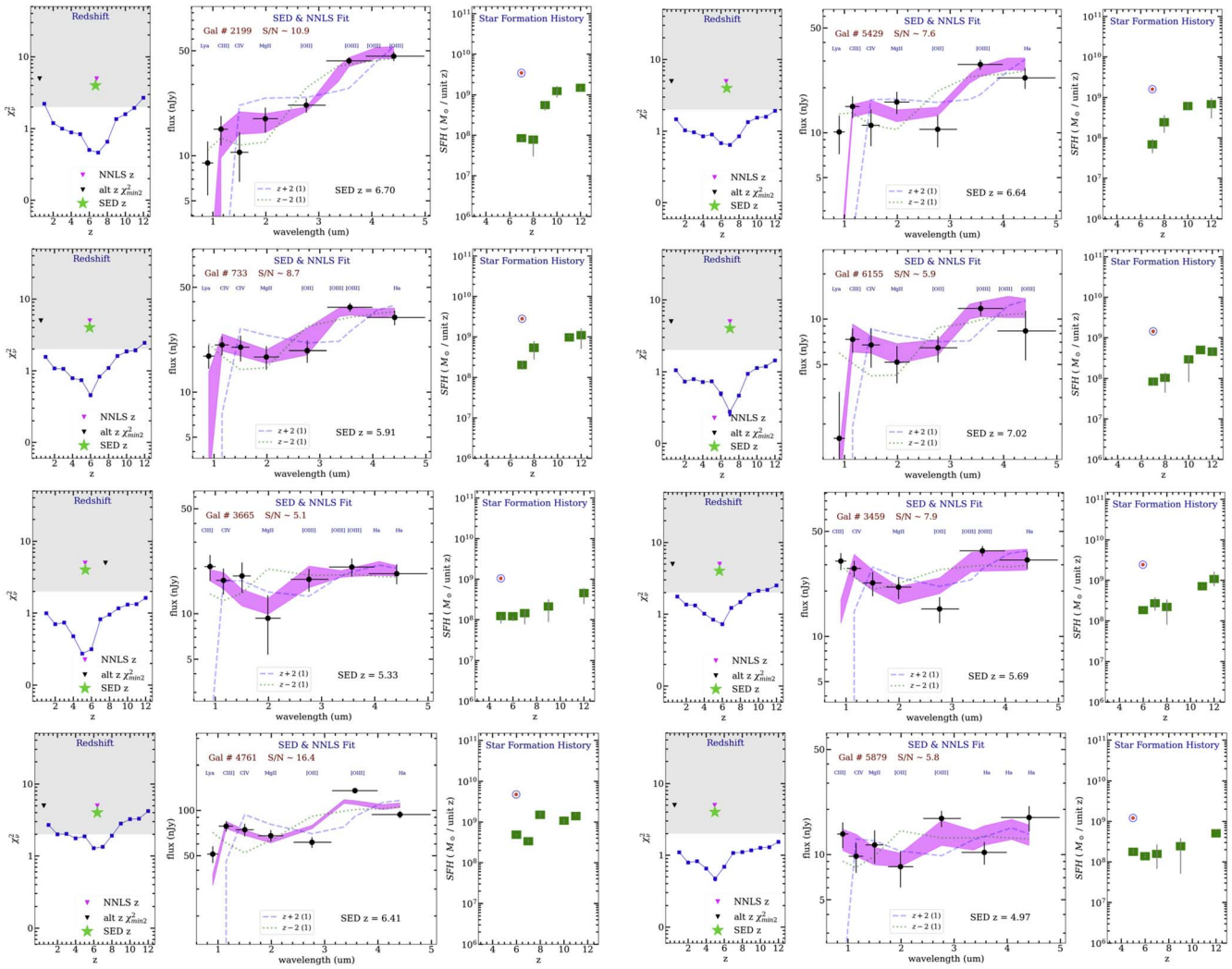

Figure 3. Examples of galaxies dominated by long, often continuous SFHs extending back to $z = 11$–12, either level or declining. There are several cases of order-of-magnitude changes in stellar mass added (more or less), but most of the data are consistent smooth SFHs. These are not the most common SFHs in our sample; galaxy 4144, not shown, is the only additional example. Panels, lines, and symbols are the same as in Figure 1.

formation and growth, and appear to have been forming stars continuously from $z \sim 12$. There are indications of abrupt order-of-magnitude changes in stellar mass added (more and less), but mostly they are smooth SFHs.

In the sample of 33 galaxies, there are no extended, rising SFHs. However, this is consistent with the results of our simulations of stochastic SFHs (Appendix A), which show the difficulty of detecting an old, fading population behind the light of an ascending, younger population (e.g., Iyer et al. 2020; Whitler et al. 2023). On the other hand, many of the falling SFHs with shorter runs of contiguous star formation (see Figure 5) could be masking rapidly rising star formation prior to their detection. Larger and deeper samples will be needed to characterize such behavior and, in general, the distribution of SFH types through what will essentially be continuity constraints.

A more thorough inspection of the SEDs themselves in Figure 3 reveals that all have a substantial older stellar population, in agreement with the derived SFHs. Also consistent is the absence of strong emission lines (raising the flux in a wide band) that has been seen in some of the stochastic or burst-dominated cases we look at next.

Figure 4 shows examples of galaxies with what look like more stochastic SFHs—bursty, repeating, and noncontinuous episodes of <200 Myr. The top two cases are a single and perhaps an extended single burst. The third and fifth examples are galaxies with widely separated bursts of star formation. Each formed roughly half of their stellar mass at $z = 11$–12, then experienced a comparatively quiescent period with a comparable burst of star formation added near OE; possibly these are interrupted versions of the long SFHs of Figure 3. The blue upturn of each SED relative to longer wavelengths is representative of the younger, ongoing star formation added to a much older population, with little in between.

The fourth and sixth examples are two nearly identical triple bursts (with a mass difference of a factor of 3) that look like (at least for the two pairs of early bursts) independent events, possibly followed by decaying star formation for each at the following (adjacent) epoch. The strong resemblance of the SEDs and SFHs for these two cases demonstrates the strong SED $\langle - \rangle$ SFH relation for the $5 < z < 12$ galaxies that SEDz* exploits. The last two panels show two SFHs that suggest extended star formation episodes—three and four starbursts spread over a few hundred megayears, continuous or episodic.

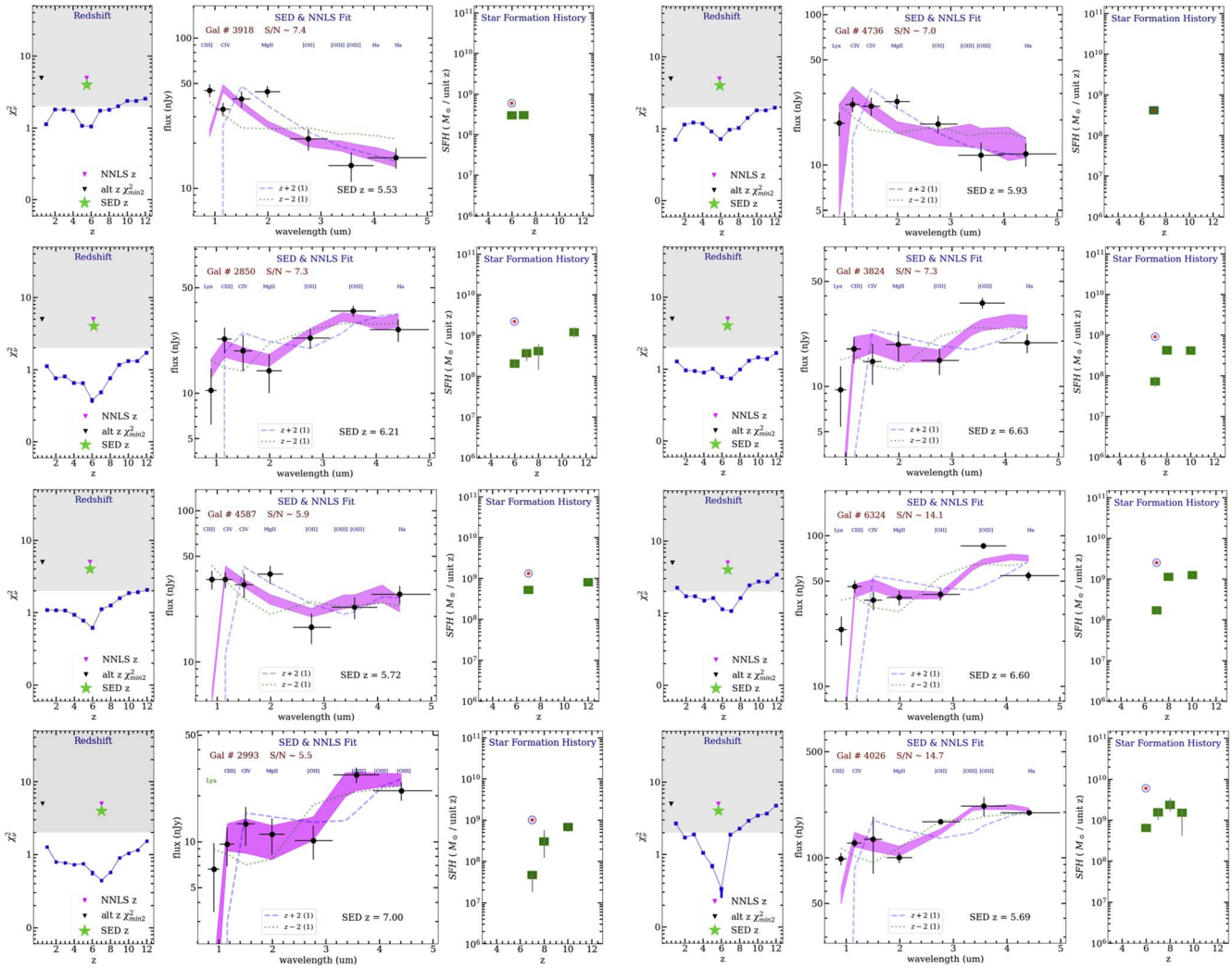

Figure 4. Examples of galaxies characterized by bursty or widely separated episodes of star formation. The star formation episodes of the top two appear to be single bursts of $\sim 5 \times 10^9\ M_\odot$; five others of the 33 galaxy sample resemble these. Further examples appear to be multiple bursts that could be associated (see text). Panels, lines, and symbols are the same as in Figure 1.

These might be cases of extended burst histories, but, according to the tests done for Figures 8 and 9 of Appendix B, they could possibly be single early single bursts, $z = 9$ and 10, that are badly resolved by the SEDz* fitting of the SED. Arguing against this interpretation is star formation at OE in both cases, unlike the typical simulated cases in Figure 8.

Lastly, Figure 5 shows further diversity in high-redshift SFHs. All eight are examples of a "run of star formation" over three adjacent epochs, typically at $z = 8 - 7 - 6$. As just discussed, a detection by SEDz* of adjacent episodes of star formation at higher redshift observed in a galaxy at much lower redshift (e.g., $z = 5$ or 6) may only be a failure to resolve a single, larger burst. Unlike those, however, for six of the eight cases we show in Figure 5, star formation is spread over lower redshifts. The epochs of 8, 7, and 6 have durations of 125, 171, and 244 Myr, over which time the SED changes markedly, which means that their SFHs are not easily confused with bursts, for example. Rather, these half-gigayear runs of star formation producing between 5×10^8 and $5 \times 10^9\ M_\odot$ by redshifts 5–6 could be the beginnings of typical M^* galaxies. The lack of rising star formation before these usually declining, short SFHs is interesting, since at these epochs, lower rates at $z \sim 9$, for example, should be detectable. A possibility is that the first episode of these short SFHs is a burst lasting only tens of megayears, unresolved in the ~100 Myr of the first epoch.

The presence of both short and long continuous runs of star formation, along with a diversity of starbursts also occurring over short or long timescales, suggests that the starburst examples are undergoing significant merger events, while the continuous SFHs, whether short or long, suggest galaxies left largely undisturbed through their early growth.

We note that, given the heterogeneous nature and varying quality of this early sample, we have not tried to estimate the frequencies of the different types of SFHs identified. However, for what it is worth, the three types of SFHs in Figures 3, 4, and 5, including the cases in the 33 galaxy sample that are not shown, amount to 27%, 45%, and 27%, a roughly uniform distribution, with bursty behavior leading the way.

5. Summary and Future Work

The principal goal of this paper has been to show how broadband imaging with NIRCam on JWST can provide an excellent measurement of both redshift and SFH; the latter is critical to understanding the assembly of the earliest galaxies.

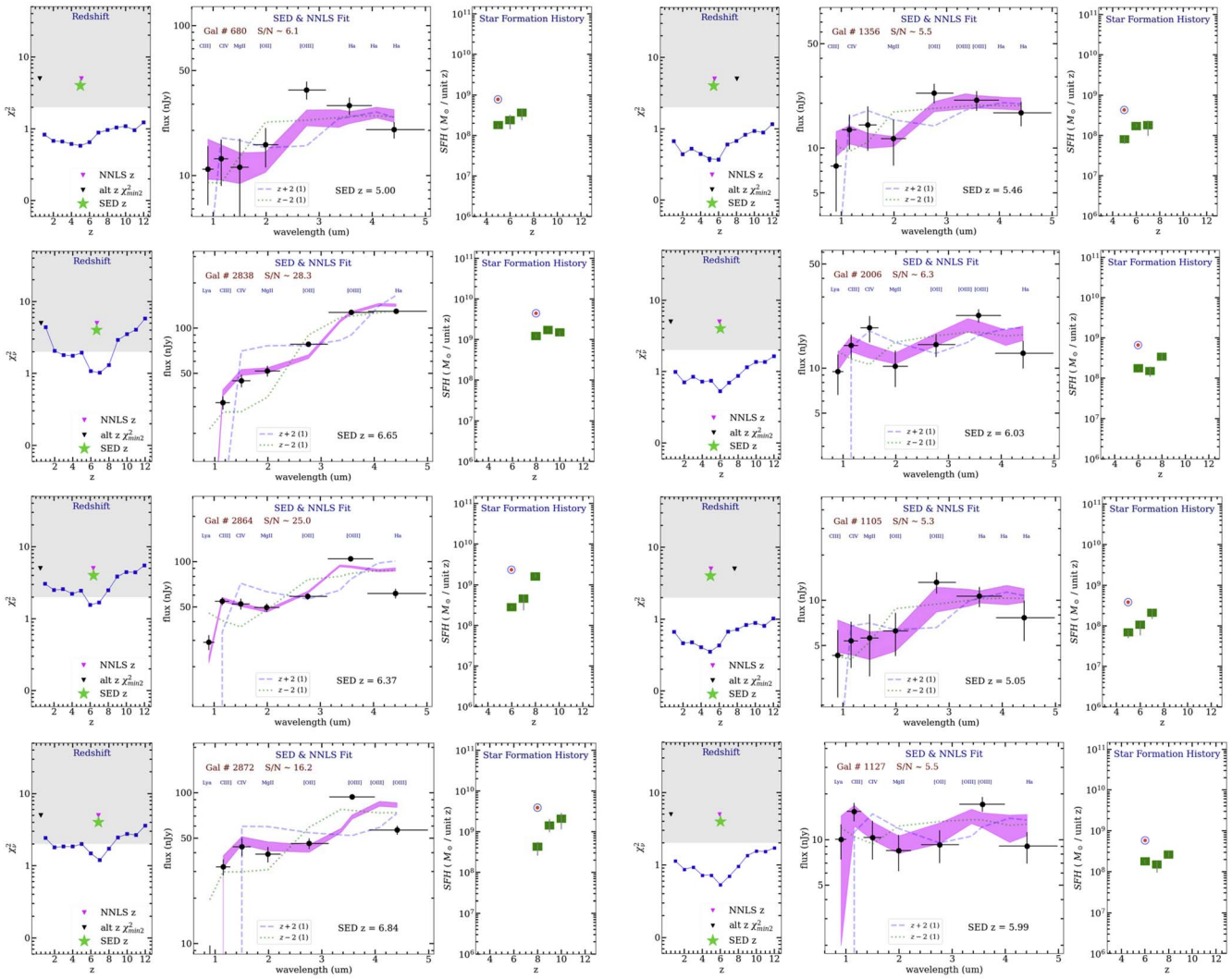

Figure 5. Examples of galaxies characterized by the most common type of SFHs found in this early study: runs of star formation over three contiguous epochs. This might be how the most common M^* galaxies are born and grow. Panels, lines, and symbols are the same as in Figure 1.

High-redshift SFHs will also provide an additional probe of galaxy populations at $z = 11$–12 and possibly beyond; the SFH of each lower-redshift galaxy probes earlier times, adding to what we will learn from actually observing galaxies at that time.

Future data will include deeper NIRCam imaging with more multiple, highly dithered images that will minimize cosmetic defects and improve photometric measurements; uniformity in all bands is critically important for SED analysis. Improvements in S/N and defect-free imaging will be crucial for optimizing the ability of SEDz* to delineate and distinguish SFHs for the first galaxies.

This initial small sample appears to exhibit the types of SFHs that astronomers would expect, including falling SFHs ("tau models") leading to the near-constant star formation rate that dominates the epoch of greatest growth, $z \sim 3 \rightarrow 1$. But even this small sample suggests that starbursts (stochastic histories) and as-yet-undetected rising SFHs—expected to dominate as we look further back to "the beginning"—are showing up. If the results of this study are indicative of what is to come, astronomers can look forward to the JWST fulfilling its "prime" mission better and sooner than we could have hoped.

A.D. gratefully acknowledges the support of the NIRCam team for the opportunity to contribute to the NIRCam science program on the earliest galaxies. The DC2 "deep field" simulation was a Herculean task that provided the essential guidance for the program described here and the NIRCam GTO program to come. A.D. also thanks the GLASS team for allowing him in, to lift the curtain on the growth of the first galaxies—what the "HST & Beyond" Committee (Dressler et al. 1996) dared to dream.

This work is based on observations made with the NASA/ESA/CSA James Webb Space Telescope. The data were obtained from the Mikulski Archive for Space Telescopes at the Space Telescope Science Institute, which is operated by the Association of Universities for Research in Astronomy, Inc., under NASA contract NAS 5-03127 for JWST. These observations are associated with program JWST-ERS-1324. The JWST data used in this paper can be found on MAST at DOI: 10.17909/fqaq-p393. We acknowledge financial support from NASA through grant JWST-ERS-1324. D.S., K.M., M. R., and A.D. are supported by JWST/NIRCam contract to the University of Arizona NAS 5-02015. A.M. acknowledges financial support through grant PRIN-MIUR 2017WSCC32.

Appendix A
Testing SEDz* with Simulated SFHs

In this Appendix, we show examples of simulations of SFHs that have been used to test the robustness of the resulting SFH. We first show how the basic types of SFHs we find can be validated by the simulation process by examining six "generated" examples. In Appendix B, we address the uniqueness of the SEDz* solutions, specifically, the robustness of the long SFHs of Figure 3 and the possibility that some or all of these could actually be bursty SFHs misidentified by SEDz*.

The SEDz* program solves for the buildup in stellar mass per epoch by finding a maximum-likelihood solution of the observed SED from combinations of stellar population templates. The process is reversible because of the strong covariance of SFH and SED over the first gigayear of cosmic history. Our tests of SEDz* consist of "composing" SFHs, like the green squares in Figures 3, 4, and 5, over $5 < z < 12$ and then using SEDz* "backward" to construct the SED that generates the invented mass profile. This has been done for parametric SFHs, such as smooth rising or falling SFHs over many epochs as well as shorter connected epochs of star formation or bursts. The three steps are (1) invent SFHs like those observed in the figures, (2) use the SEDz* code in reverse to produce the SED that would generate the simulated SFH, and (3) use SEDz* to generate 21 SFHs by perturbing the SED by expected random errors, including error bars on the green boxes to represent the quartile ranges of those 21 solutions. Comparing the simulated and recovered SFH tests the fidelity of the code.

Figure 6 shows six examples. The dark blue dots are the "invented" run of stellar mass, and the small red dots are the integrated mass; the green dot with a red ring indicates the total accumulated mass. In all cases, the simulated mass buildup is well traced by the recovered mass growth, even as the epoch-to-epoch agreement bounces around, as would be seen in the evolution of this diagram stepped through earlier epochs than those shown in this Appendix and Figure 6 (we show examples of this epoch-by-epoch buildup in Figure 7).

The top three histories were constructed to resemble those of Figure 3: long, falling, mostly continuous runs of star formation since $z = 11$ or 12. We show, top left to right, CSF until $z = 6$ or 5. In these cases, the star formation is added in 10 Myr bursts only; there is no constant star formation at OE.[23] The example on the right was designed to be smooth and declining with a stochastic "noise" of a factor of ∼2, similar to the steeper examples in Figure 3. The middle panel of Figure 3 shows a slightly rising SFH that is recovered as slightly falling, and for the right example, the modestly rising SFH that is simulated is recovered as flat. In summary, the basic character of a long stretch of star formation is recovered, but the slopes are not accurate. This is unimportant for our purposes here, but it suggests that it might be necessary to see what systematic error produces the effect and possibly adjust for it.

The qualitative agreement is good for these top-row examples; the smoothness and falling character are recovered, although in each case, the SFH is higher earlier and lower later than what was simulated. The typical scatter of a factor of 2 comparing model (purple points) and recovered masses (green squares) is remarkably good and certainly sufficient for a basic description of the SFH—the goal of this program.

The bottom panels are simulations of different degrees of bursty behavior. The bottom left case simulates three independent bursts, $10^9\ M_\odot$ at $z = 12$, $3 \times 10^9\ M_\odot$ at $z = 9$, and $6 \times 10^8\ M_\odot$ at $z = 7$. The agreement is good, except for the alias mass added at $z = 10$. These simulations suggest that SFHs dominated by bursts, like those in Figure 4, are well recovered by SEDz*. Again, the displacement of the points from the model by factors of 2 is insignificant our purpose.

The example in the middle panel is for the kinds of shorter but continuous runs of star formation shown in Figure 5. Again, the agreement is qualitatively very good, with a slight systematic error in slope. Another alias is seen at $z = 11$, well before the simulated SFH.

Finally, the bottom right example is for a simulation of four episodes of star formation that are disjoint but likely associated: $2 \times 10^9\ M_\odot$ at $z = 10$, $8 \times 10^8\ M_\odot$ at $z = 8$, and two at $\sim 10^8\ M_\odot$ at $z = 7$ and 6. Again, there is a slope error, scatter, and an alias at $z = 9$, but the character of the SFH is recovered successfully.

Our more extensive simulations, like those in Figure 6, show that SEDz* is successful at recovering the basic form of a wide variety of SFHs. With more experience and understanding of how to optimize this kind of testing and a richer, deeper sample than is now available, SEDz* should be able to characterize the distribution of SFHs and perhaps even how the distribution itself evolves over the epoch $5 < z < 12$.

[23] In the normal running of SEDz*, bursts serve as the normal way of adding mass to the galaxy; only at OE is the burst resolvable into a component of relatively young stars, but by the next epoch, the burst cannot be distinguished from constant star formation over the previous epoch and is suitable for building up a old stellar population.

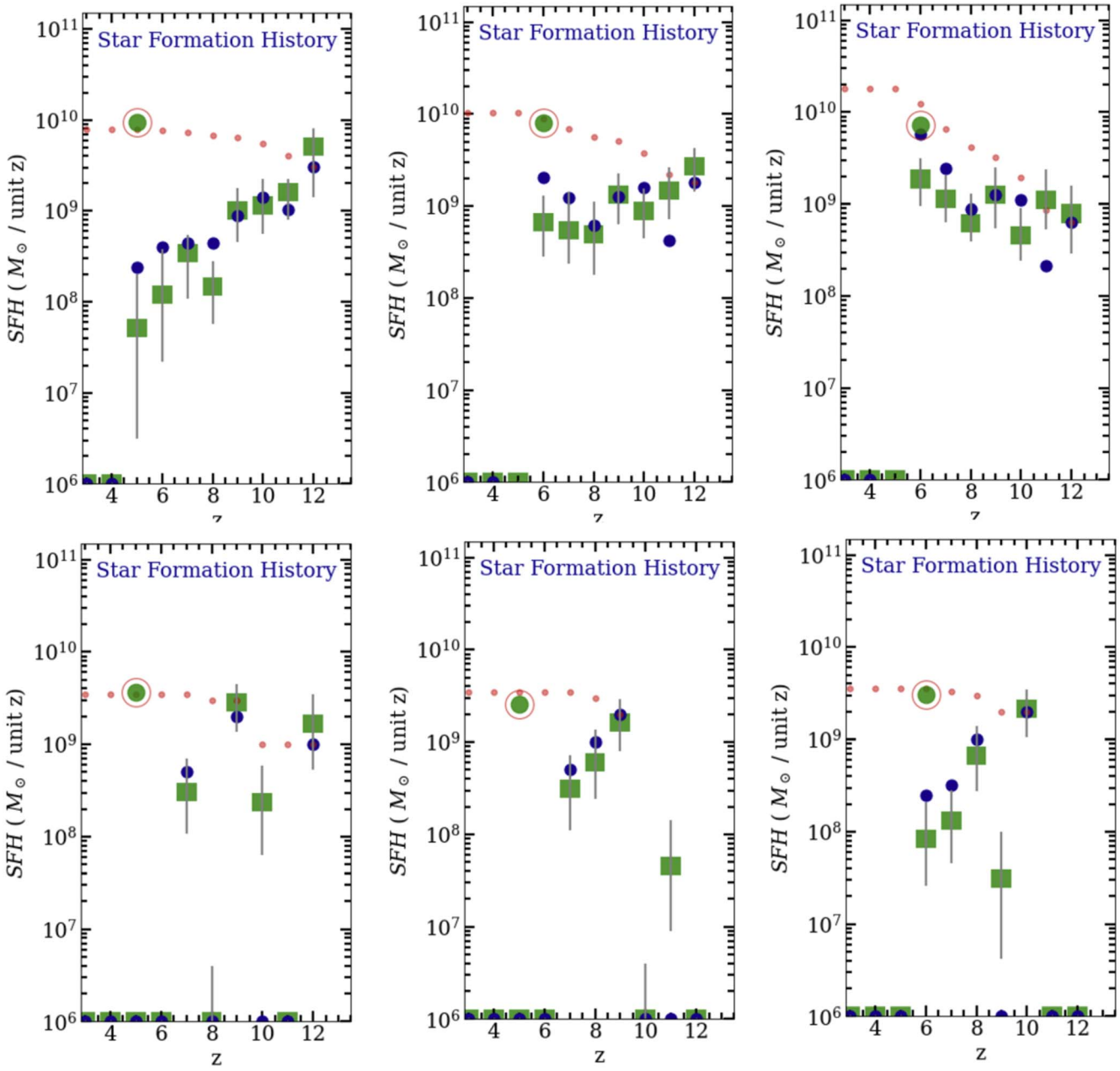

Figure 6. Validation of the SEDz* code through simulations. Each panel shows a different input SFH (dark blue dots) and how the code retrieves it (green squares) through SED fitting. Red dots show the integrated mass at each step, with a green dot with a red ring marking the total mass. Details of the characteristics of the different input SFHs are given in Appendix A.

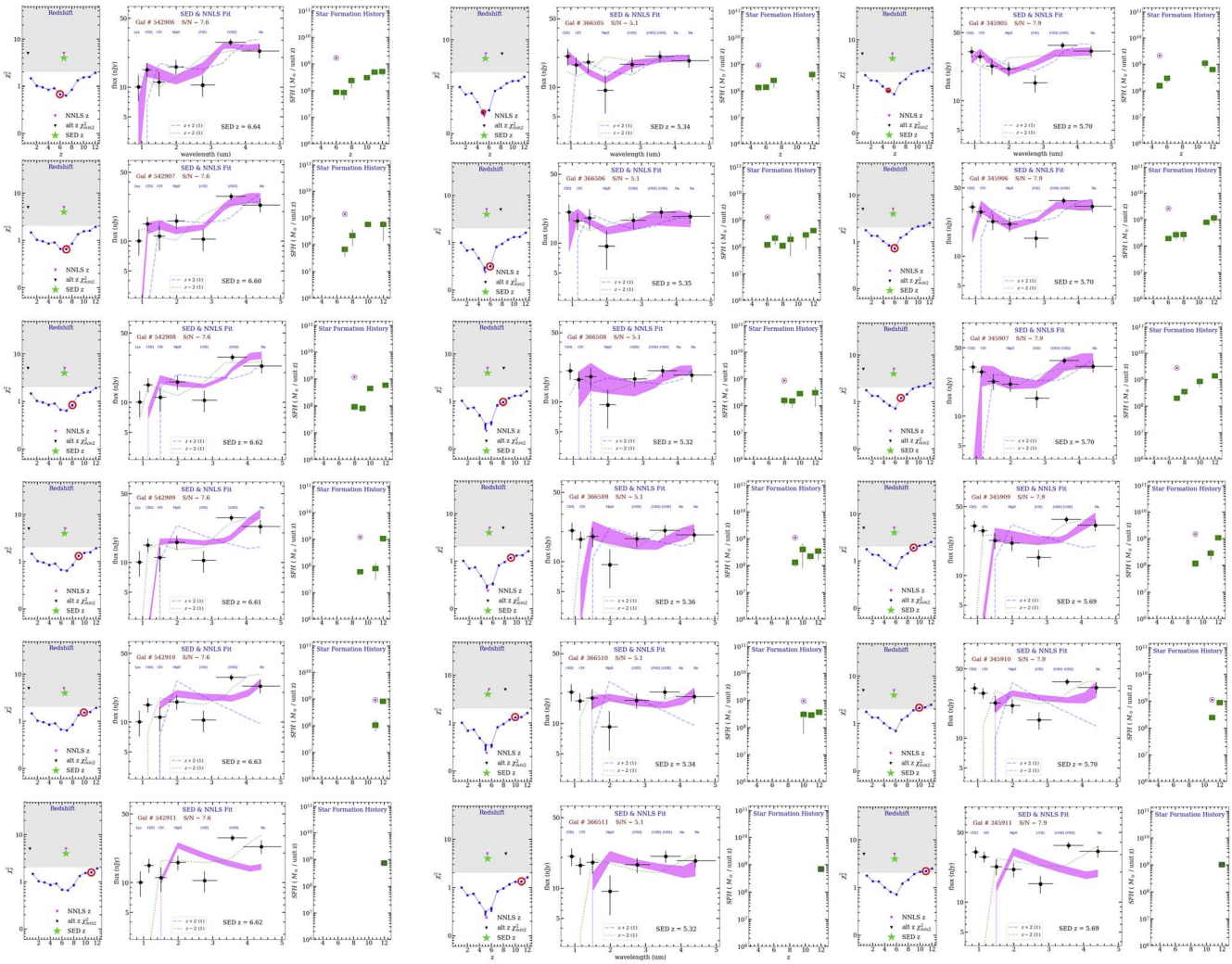

Figure 7. "Growth history" of three of the eight galaxies in Figure 3, showing a long, mostly continuous star formation from $z = 12$. These three—GLASS-5429, GLASS-3665, and GLASS-3459—are representative of all eight. We plot the operation of SEDz* epoch by epoch to show how contributions from each stellar population are calculated by NNLS, combining stellar population templates and steadily improving $\tilde{\chi}^2$ from the poor fit of the observed SED using star formation only from the earliest epochs (starting at the bottom with $z = 11$) to the excellent fit of the SED at the top of each of the three columns (OE). Panels are labeled by galaxy number + epoch; for example, "G366508" is the best-fit SED produced by adding stellar templates up from $z = 12$ to 8. The red ring in each $\tilde{\chi}^2$ plot denotes the epoch of that frame. For GLASS-5429, the minimum $\tilde{\chi}^2 = 0.8$ is reached at an OE of $z = 5$.

Appendix B
How SEDz* Builds the "Best" SFH

The purpose of this section is to use simulations to further illustrate how SEDz* computes an SFH by combining fluxes from stellar population templates to find the best fit to an observed SED. Specifically, we show that SEDz* finds a unique solution that is the best measurement of the SFH and related uncertainties, free of preconceptions or bias of what that SFH might be.

We begin this section by exploring, epoch by epoch, the SFHs of galaxies shown in Figure 3 that we described as having long and more or less continuous star formation for the ~1 Gyr $z = 12$ to OE ($5 < z < 7$). In Figure 7, we show in three columns three examples from Figure 3: GLASS-5429, GLASS-3665, and GLASS-3459. For each, star formation begins at or before $z = 12$ and accumulates by OE to ~ 1–$2 \times 10^9\ M_\odot$. As we described in Section 2, SEDz* uses two sets of stellar population templates, for 10 Myr bursts and CSF, with fluxes recorded at integer redshifts $z = 12$–3. For each epoch, these "template tables" give the fluxes expected from 1 $M_\odot\ \mathrm{yr}^{-1}$ at that redshift and the subsequent fluxes for that evolving population.

Each of the three tests begins with the bottom panel, with OE at $z = 11$, and works up to an OE of $z = 6$ (left case) or 5 (middle and right cases). Using GLASS-5429 (left) as an example and starting at the bottom, SEDz* has attempted to fit the observed SED (OE, $z = 6$) only with stars born at $z = 12$ and 11. The best fit is for a mass of 9×10^8 (right panel) at $z = 12$ and no $z = 11$ contribution, producing an SED (magenta line, middle panel) that is a very poor fit to the observed NIRCam fluxes (black points with errors), as indicated by inspection and the high $\tilde{\chi}^2$ (left panel).[24] The next epoch up shows the best fit at $z = 10$ and demonstrates a key feature of SEDz*: the previous $z = 12$ and 11 contributions are not simply "carried over" to $z = 10$. Instead, these are recomputed with new mass estimates for the evolved fluxes from $z = 12$ and 11 star formation and adding more at $z = 10$. In other words, the

[24] In this case, there is no contributed star formation at $z = 11$ because its SED would be moderately blue, so there is no amount that would improve the fit to the moderate age population of the observed SED.

amplitude of star formation at each previous epoch and the "present" epoch are vectors that the NNLS weighs and combines to find the lowest $\tilde{\chi}^2$. The fit at $z = 10$ to the observed SED is a bit better, and this improvement continues up the sequence of epochs as star formation is added at $z = 9$, 8, and 7. The best fit—the lowest $\tilde{\chi}^2$—that sets the redshift of the SED derives from contributions from most epochs. This contrasts with the situation for bursty SFHs, discussed in the next section.

The other two cases shown here, GLASS-3665 and GLASS-3459, show the same behavior; the good fit of the SED at the minimum $\tilde{\chi}^2$ develops from $z = 11$ as additional epochs of star formation are added. These three examples are typical of the full sample of eight galaxies shown in Figure 3; this "continuing growth" behavior played no role in their inclusion in our sample and indeed was not recognized before this "evolution of the SED" experiment. This is our primary evidence that the long, continuous SFHs in Figure 3 are genuine; achieving the best fit requires the addition of stellar populations over a wide redshift range.

Appendix C
Can SEDz* Mistake Bursts for Long SFHs?

In the previous section, we used SFH simulations to show that the long SFHs we have found are, in fact, reproduced by star formation over most of the epochs $z = 12$–5. Of course, some of these might be better described as a series of four to five bursts with significant drops in star formation in between. Since SEDz* cannot resolve such star formation episodes, a better way to answer this question could be to use a large sample to study the distribution of bursty histories to see if there is a continuum of SFHs that varies between one or two bursts from $z = 12$–5 and the long histories just discussed. Lacking such a sample at this time, it is useful to ask if well-separated bursts can mimic long histories, at least to the extent that most or all of the examples in Figure 3 could be "noisy" versions of bursts. We investigate this question in this section.

We rigged the SEDz* simulation program to produce random combinations of bursts with masses between $10^{8.5}$ and $10^{9.5}$ $M_{\odot}$; redshifts $z = 8$, 9, 10, 11, or 12; and observed at $z = 5$, 6, or 7. Fifty such combinations were made; the first 28, which are representative, are shown in Figure 8. For each combination, there is a pair of SEDz* plots: the burst parameters at the chosen epoch (top) and a companion SFH at the chosen OE (bottom).[25] Scanning over these examples, it is readily seen that, at the redshift of the burst, the SFH is usually a single epoch or two adjacent epochs of star formation, and the observed starburst from a much later time is unresolved and typically splits into several epochs straddling the input epoch of the burst. At OE, the SED is always steep for these; there is no star formation that extends to OE at a significant level, so the relatively old population dominates.

However, there are six cases out of 28 where we see something like the long SFHs of Figure 3, simulated in the previous section (examples enclosed in blue boxes). We extract these for comparison with six of the observed SFHs in Figure 9. We see that, although superficially like the long SFHs on the right, there are differences. Simulations 6, 14, 16, and 26 all have flat SFHs around the burst epoch (the "resolution" problem), with two rapidly falling values—with large error bars—to lower redshift. GLASS 2199 on the right is the closest to these in steepness, but its longer history is distinguishable. Simulations 8 and 15 are most like the righthand examples, which would make this possibility a $<10\%$ occurrence. In point of fact, there is another difference that separates even these mistaken burst SFHs from the examples in Figure 3: their SEDs are all considerably redder (with the exception of GLASS 2199). As expected, the SED of an old burst is not likely to mimic an SFH that has a significant proportion of relatively younger stars.

We conclude from this test that a small fraction of strong bursts at higher redshift can appear to stretch to longer histories when viewed at $z = 5$–7, but they could only account for at most one or two of the long SFHs we have identified; because of the difference in the SED color, even these should be distinguishable.

Reviewing these tests, Figure 6 shows that we can simulate SFHs of the kinds seen in this paper and recover them with sufficient fidelity to distinguish one type from another. Figure 7 shows that the long SFHs we observe extending to lower z are in fact resolved by SEDz* into many epochs of star formation from $z = 12$ to OE. Figures 8 and 9 show through simulations that $8 < z < 12$ bursts are unlikely to be mistaken for long SFHs. Even if a burst cannot be pinned down to a certain redshift and duration when viewed from $5 < z < 7$, its derived SFH does not contaminate the sample of the other histories we have shown; it is identifiable as a likely burst in most cases. The ability of SEDz* to leverage stellar populations whose light is dominated by A stars to investigate the variety of SFHs at $z > 5$ is confirmed.

[25] The attentive reader will notice that these $\tilde{\chi}^2$ fits are extraordinarily sharp; this is an artifact of using the same templates to compose an SFH and for regenerating the SFH, in contrast to the situation with real data, where stellar populations are compared to templates.

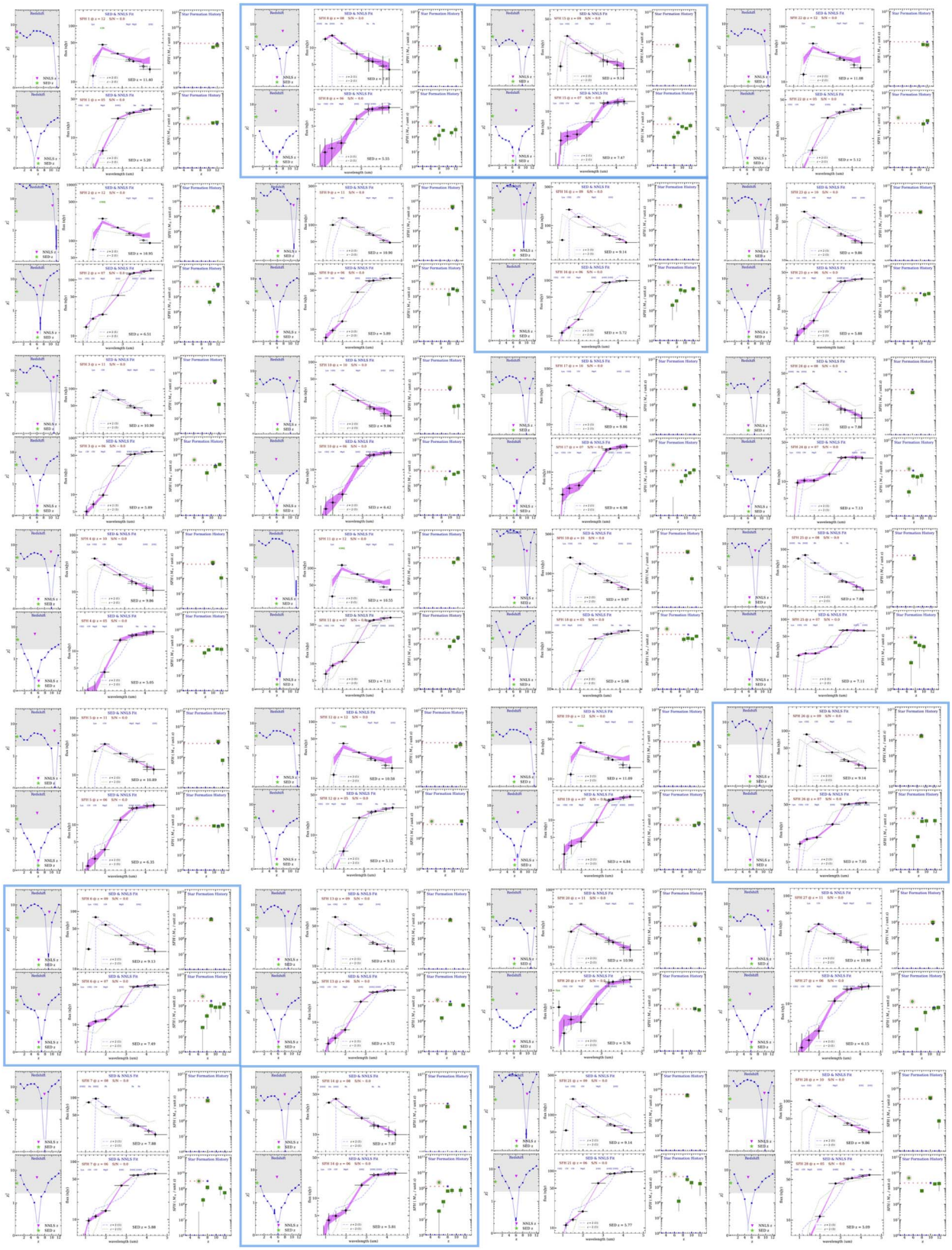

Figure 8. Twenty-eight out of 50 simulations of bursts at $10^{8.5}$ and $10^{9.5}$ $M_{\odot}$; redshifts of $z = 8$, 9, 10, 11, or 12; and observed at $z = 5$, 6, or 7. For each pair, the SEDz* plot of the burst epoch (top) is compared to the OE (bottom). The SFH of the burst is usually resolved as one or two epochs at the burst redshift, and this commonly spreads to an unresolved three or four epochs around the burst redshift when viewed later, at OE. However, six of the 28 examples (enclosed in blue boxes) do show histories that appear to continue down almost to OE, presenting the appearance of a long SFH. But, in contrast to the observed long SFHs of Figure 3, a burst SED seen at OE is always red; it is an old stellar population lacking later star formation to moderate its color (see Figure 9). (Note that in the "simulation" plots, total mass is marked by a green dot with a red ring.)

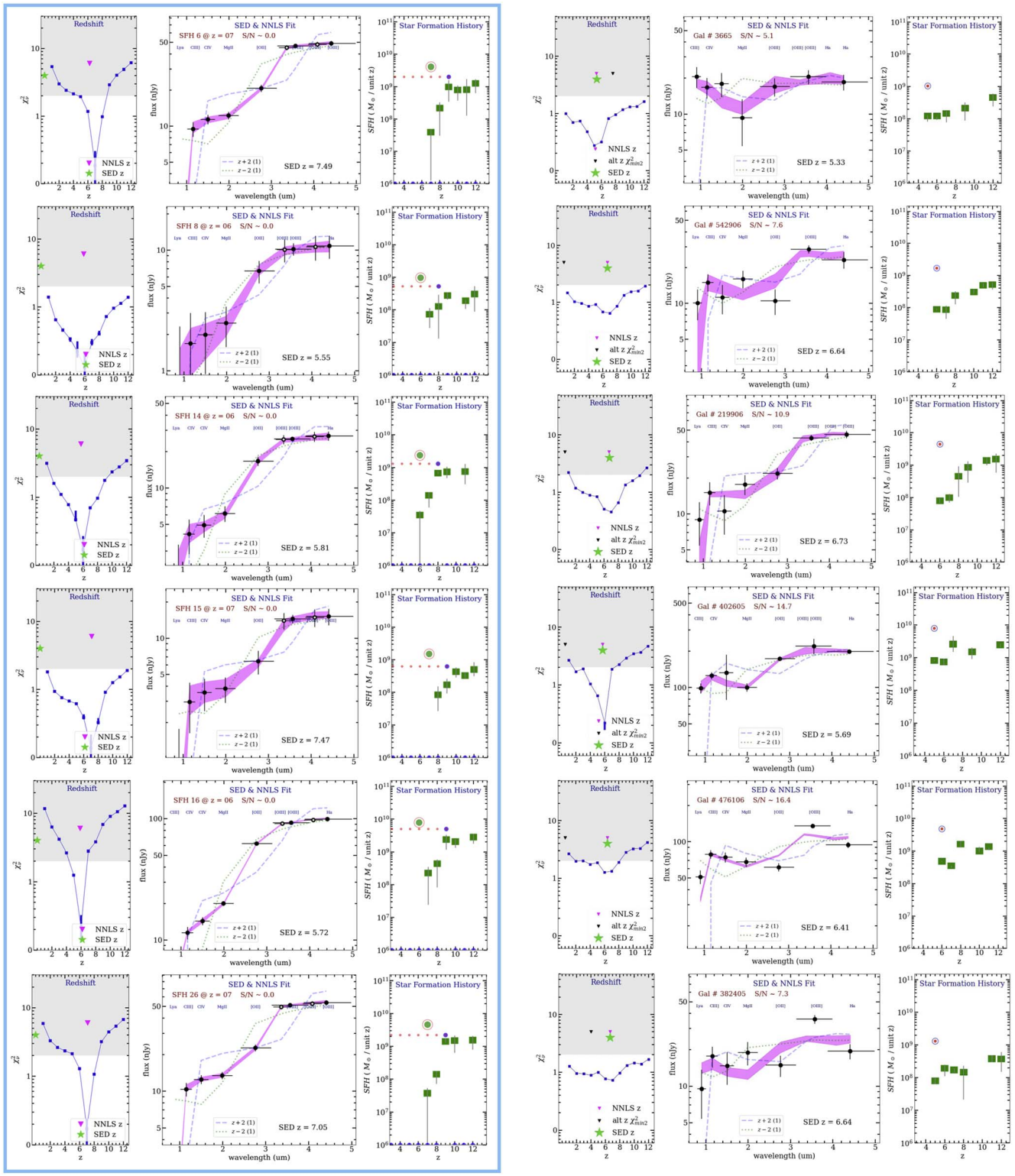

Figure 9. Left: six best examples of simulated higher-redshift bursts that might be mistaken for longer SFHs. (Total mass is marked by a green dot with a red ring.) Right: six observed examples from Figure 3, for comparison. (Total mass is a red dot with a blue ring.) In addition to being a small fraction of the burst simulations, the impersonators are distinguishable by their flat starts/steep falloffs in star formation, in contrast to the steady declines seen in the observed sample, and their steeper SEDs, which come naturally from the domination of older stellar populations.

ORCID iDs

Alan Dressler https://orcid.org/0000-0002-6317-0037
Benedetta Vulcani https://orcid.org/0000-0003-0980-1499
Tommaso Treu https://orcid.org/0000-0002-8460-0390
Marcia Rieke https://orcid.org/0000-0002-7893-6170
Antonello Calabrò https://orcid.org/0000-0003-2536-1614
Marco Castellano https://orcid.org/0000-0001-9875-8263
Adriano Fontana https://orcid.org/0000-0003-3820-2823
Nicha Leethochawalit https://orcid.org/0000-0003-4570-3159
Charlotte Mason https://orcid.org/0000-0002-3407-1785
Emiliano Merlin https://orcid.org/0000-0001-6870-8900
Takahiro Morishita https://orcid.org/0000-0002-8512-1404
Diego Paris https://orcid.org/0000-0002-7409-8114
Marusa Bradac https://orcid.org/0000-0001-5984-0395
Amata Mercurio https://orcid.org/0000-0001-9261-7849
Themiya Nanayakkara https://orcid.org/0000-0003-2804-0648
Bianca M. Poggianti https://orcid.org/0000-0001-8751-8360
Paola Santini https://orcid.org/0000-0002-9334-8705
Xin Wang https://orcid.org/0000-0002-9373-3865
Christopher Willmer https://orcid.org/0000-0001-9262-9997

References

Aparicio, A., & Hidalgo, S. L. 2009, AJ, 138, 558
Baade, W. 1951, POMic, 10, 7
Barrufet, L., Oesch, P. A., Weibel, A., et al. 2022, arXiv:2207.14733
Brammer, G. B., van Dokkum, P. G., & Coppi, P. 2008, ApJ, 686, 1503
Bruzual, G., & Charlot, S. 2003, MNRAS, 344, 1000
Castellano, M., Fontana, A., Treu, T., et al. 2022, ApJL, 938, L15
Chevallard, J., & Charlot, S. 2016, MNRAS, 462, 1415
Cignoni, M., & Tosi, M. 2010, AdAst, 2010, 158568
Couch, W. J., & Sharples, R. M. 1987, MNRAS, 229, 423
Dalcanton, J. J., Williams, B. F., Melbourne, J. L., et al. 2012, ApJS, 198, 6
Dalcanton, J. J., Williams, B. F., Seth, A. C., et al. 2009, ApJS, 183, 67
Diemer, B., Sparre, M., Abramson, L. E., & Torrey, P. 2017, ApJ, 839, 26
Dressler, A., Brown, R. A., Davidsen, A. F., et al. 1996, Exploration an the Search for Origins: A Vision for Ultraviolet-Optical-Infrared Space Astronomy, Technical Report, HST & Beyond Committee
Dressler, A., & Gunn, J. E. 1983, ApJ, 270, 7
Dressler, A., Kelson, D. D., & Abramson, L. E. 2018, ApJ, 869, 152
Fan, X., Strauss, M. A., Becker, R. H., et al. 2006, AJ, 132, 117
Finlator, K., Oppenheimer, B. D., & Davé, R. 2011, MNRAS, 410, 1703
Gallart, C., Aparicio, A., Bertelli, G., & Chiosi, C. 1996, AJ, 112, 1950
Gladders, M. D., Oemler, A., Dressler, A., et al. 2013, ApJ, 770, 64
Iyer, K. G., Tacchella, S., Genel, S., et al. 2020, MNRAS, 498, 430
Jaacks, J., Finkelstein, S. L., & Bromm, V. 2018, MNRAS, 475, 3883
Johnson, B. D., Leja, J., Conroy, C., & Speagle, J. S. 2021, ApJS, 254, 22
Kelson, D. D., Benson, A. J., & Abramson, L. E. 2016, arXiv:1610.06566
Kelson, D. D., Williams, R. J., Dressler, A., et al. 2014, ApJ, 783, 110
Lawson, C., & Hanson, R. 1995, Solving Least Squares Problems. Classics in Applied Mathematics (Philadelphia, PA: SIAM)
Leethochawalit, N., Trenti, M., Santini, P., et al. 2022, arXiv:2207.11135
Mason, C. A., Trenti, M., & Treu, T. 2022, arXiv:2207.14808
Merlin, E., Bonchi, A., Paris, D., et al. 2022, ApJL, 938, L14
Morgan, W. W., & Keenan, P. C. 1973, ARA&A, 11, 29
Nanayakkara, T., Glazebrook, K., Jacobs, C., et al. 2022, arXiv:2207.13860
Oemler, A. J., Dressler, A., Gladders, M. G., et al. 2013, ApJ, 770, 63
Planck Collaboration, Adam, R., Aghanim, N., et al. 2016, A&A, 596, A108
Poggianti, B. M., Smail, I., Dressler, A., et al. 1999, ApJ, 518, 576
Robertson, B. E., Ellis, R. S., Dunlop, J. S., McLure, R. J., & Stark, D. P. 2010, Natur, 468, 49
Santini, P., Fontana, A., Castellano, M., et al. 2022, arXiv:2207.11379
Stark, D. P., Schenker, M. A., Ellis, R., et al. 2013, ApJ, 763, 129
Tacchella, S., Finkelstein, S. L., Bagley, M., et al. 2022, ApJ, 927, 170
Tolstoy, E., & Saha, A. 1996, ApJ, 462, 672
Tosi, M., Greggio, L., & Focardi, P. 1989, Ap&SS, 156, 295
Treu, T., Calabro, A., Castellano, M., et al. 2022b, arXiv:2207.13527
Treu, T., Roberts-Borsani, G., Bradac, M., et al. 2022a, ApJ, 935, 110
Whitler, L., Endsley, R., Stark, D. P., et al. 2023, MNRAS, 519, 157
Williams, C. C., Curtis-Lake, E., Hainline, K. N., et al. 2018, ApJS, 236, 33
Worthey, G. 1994, ApJS, 95, 107
Yang, L., Morishita, T., Leethochawalit, N., et al. 2022, ApJ, 938, L17